

Similarities between Active and Magnetically-Actuated Flagella of Sperm Cells

Resemblance between Motile and Magnetically-Actuated Sperm Cells

Islam S. M. Khalil^{1, a)}, Veronika Magdanz^{2, b)}, Juliane Simmchen,³ Anke Klingner,⁴ and Sarthak Misra^{1, 5}

¹⁾Department of Biomechanical Engineering, University of Twente, Enschede, 7522 NB, The Netherlands

²⁾Applied Zoology, Faculty of Biology, Technical University of Dresden, Dresden, 01069, Germany

³⁾Physical Chemistry, Technical University of Dresden, Dresden, 01062, Germany

⁴⁾Department of Physics, the German University in Cairo, Cairo, 11835, Egypt

⁵⁾Department of Biomedical Engineering, University of Groningen and University Medical Center Groningen, Groningen, 9713 AV, The Netherlands

The active flagellum propels a motile sperm cell by travelling bending waves. Here, we demonstrate that non-motile cells have the capacity to be wirelessly actuated by external magnetic fields and reveal insights into their propulsion characteristics. Partial coating of the sperm head with nanoparticle aggregates is achieved by electrostatic-based self-assembly. The coating enables propagation of helical travelling waves along the passive flagellum under the action of a periodic magnetic field. We compare the waveforms of active and passive flagellated motion and show noticeable asymmetry in the case of magnetically-actuated cells, leading to lower linearity ($LIN = VSL/VCL$) of the taken pathway. The average curvature of the flagellar beat cycle is $10.4 \pm 8.1 \text{ rad mm}^{-1}$ (mean \pm s.d.) for an active flagellum, whereas the curvature of a passive flagellum exhibits a linear increase ($37.4 \pm 18.1 \text{ rad mm}^{-1}$) and decrease toward the distal end. We also show that the maximum amplitude of the bending wave occurs at the distal end of the active flagellum and at the middle of the passive flagellum. Our experiments also show the ability of the actuating field to control the rate of progression of the bending waves along the passive flagellum to match that of motile cells.

Keywords: flagellar propulsion, low Reynolds numbers, magnetic, sperm cell, waveform

The development of microrobots able to be wirelessly controlled has gone through two distinct methods of implementation: the geometric downscaling^{1–3} and the utilization of biological motors^{4–6}. As the size of these devices approach the microscale in the case of downscaling, it is apparent that several hurdles have to be overcome. For example, the integration of power source and propulsion mechanism are limited by the downscaling. The geometric scaling has been enabled through the wirelessly transmitted power to these devices by magnetic^{7–10}, acoustic¹¹, light¹², and chemical^{13,14} sources. Regardless of the power source, it has to be transduced into motion to propel rigid or flexible structures mostly in the shape of a helix¹⁵ or straight wire¹⁶. In either case, a propulsive force is generated by a corkscrew motion or a travelling wave to generate propulsion in low Reynolds (Re) numbers¹⁷. The second method is implemented by using a motile or non-motile microorganism or cell, either to provide propulsion¹⁸ or as a template¹⁹.

This letter studies the motion characteristics of motile and magnetically-actuated non-motile bovine sperm cells, and reveals insights into the differences between their natural and artificial rotary motors (Table I). Spermatozoa have recently been suggested as components of microrobots due to their strong flagellar driving source and ability to take up drugs^{20,21}. Further, spermatozoa navigate through the female reproductive tract regardless to fluid flow, chemicals, temperature, and near-

surface effects,^{22–24} and most existing sperm micromotors depend on the propulsive force of the active flagellum and are sensitive to physiological conditions (pH, temperature, and chemicals)²⁵. In this letter, we present the properties of magnetically-actuated passive flagella of dead sperm cells. The swimming efficacy of the magnetically-actuated cells is insensitive to these physiological conditions and lower than live cells, which is expected owing to the difference in the actuation mechanism. However, the actuation of passive flagella reveals insights into the desirable flagellar waveforms to design efficient microswimmers.

Spermatozoa perform their bending motion by switching molecular motors (dyneins) between a compression and distension state between the microtubule which are situated along the flagellum²⁶. The dynein motors are driven by ATP as energy source which is provided by the energy metabolism of the sperm cell. Sperm motion is typically analyzed using four parameters²⁷: (1) curvilinear velocity (VCL), which describes the actual sperm path; (2) average path velocity (VAP); (3) straight line velocity (VSL); and (4) linearity ($LIN = VSL/VCL$), which is a measure of the straightness of the path.

In order to experimentally compare the swimming characteristics of motile and magnetically-actuated cells, two-dimensional projections of the motion of each cell are analyzed. Non-motile cells are coated with rice grain-shaped nanoparticles at the head of the cell. A solution of $\text{FeCl}_3 \cdot \text{H}_2\text{O}$ is aged with NaH_2PO_4 for 72 hr at 100°C , resulting in positively charged elongated 100 nm iron oxide nanoparticles that adhere to the negatively charged bovine sperm cells²⁸. The magnetic moment per cell is measured by a vibrating sample magnetometer as,

^{a)}Electronic mail: i.s.m.khalil@utwente.nl

^{b)}Electronic mail: veronika.magdanz@tu-dresden.de

TABLE I. Motile and magnetically-actuated sperm cells are fluorescently labeled with green SYBR14 and red propidium iodide stains to indicate live and dead cells. Flagellum is 60 μm , head width and length are 4.5 μm and 10 μm . Scale bar is 5 μm .

	Motile sperm cell	Magnetic sperm cell
Image		
Composition	live bull sperm cell	dead bull sperm cell + nanoparticles
Actuation	ATP-driven dynein motors (active flagellum)	magnetic torque on the head (passive flagellum)
Power	energy metabolism of cell	magnetic energy from external source

$m = 1.5 \times 10^{-11}$ A m² at magnetic field of 2 mT. Sperm cells are recorded during regular beating in modified tyrode's albumine lactate pyruvate medium, and detailed shape of their active flagella is measured to quantitatively compare their waveform to magnetically-actuated passive flagella. Video recording is done with a frame rate of 500 frames per second and 640 \times total magnification and phase contrast. The shape of the flagellum is characterized by the tangent angle ($\varphi(s, t)$) enclosed between the long axis ($e_1(t)$) of the head and the local tangent along the arc-length s (Fig. 1). Fig. 1(a) shows a cell over half beat cycle, whereas Fig. 1(b) shows a magnetically-actuated sperm cell in water with viscosity ($\eta = 1$ mPa s). The actuation is achieved by applying a uniform time-dependent magnetic field and exerting magnetic torque (no magnetic force is applied) on the dipole of the cell using a tri-axial Helmholtz coil system. The cells are actuated with magnetic field ($B = 2$ mT), leading to magnetic torque on the order of 3×10^{-14} N m. The field continuously rotates in the yz -plane about the x -axis, and the head executes circular orbit leading to propagation of transverse waves along the passive flagellum. (Multimedia view)

In the case of motile cells (Fig. 1(a)), bending waves along the active flagellum are generated, and governed by the balance between the elastic and drag forces in low- Re ($\sim 10^{-4}$). The inertial forces are negligible¹⁷ and the relation between the viscous force and the velocity of a segment is linear over the beat cycle of the flagellum^{29,30}. Qualitatively similar bending waves are also generated along the passive flagellum of magnetically-actuated cells under the action of an oscillating field with the exception that they originate from magnetic torque exerted on the head. Therefore, the magnetically-actuated sperm cells are governed by the balance between the magneto-elastic and drag forces as:

$$\kappa \frac{\partial^4 \varphi}{\partial s^4}(s, t) + \xi_{\perp} \frac{\partial \varphi}{\partial t}(s, t) = 0. \quad (1)$$

The first term in equation (1) characterizes the coupling between the flagellum with bending stiffness (κ) and magnetic torque, whereas the second term describes the hydrodynamic coupling in low- Re , where ξ_{\perp} is the perpendicular drag coefficient and is considered constant owing to the low- Re characteristics^{29,30}. The flagellum

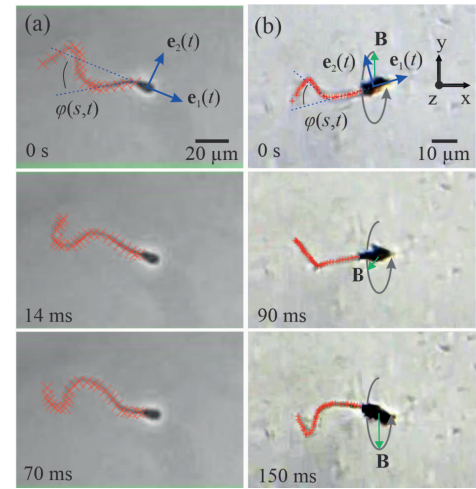


FIG. 1. Motile and magnetically-actuated sperm cells swim by travelling wave (over half beat cycle). (a) Sperm cell swims by energy metabolism ($f = 7.7$ Hz). (b) Magnetically-actuated cell swims by rotating magnetic fields ($f = 6$ Hz) about the x -axis. The field (green arrow) rotates in the yz -plane and magnetic torque is converted into propulsion. The circular gray arrow indicates the direction of rotation. The red markers indicate the tail deformation used to measure the tangent angle ($\varphi(s, t)$). (Multimedia view)

is rigidly anchored to the head with an average magnetic moment m , and the magnetic torque is specified through $\varphi(0, t) = 0$ and $\partial \varphi / \partial s(0, t) = mB \sin \omega t$. The second condition implies that the local curvature of the flagellum is controlled by the external magnetic torque and controls the propagation of harmonic waves along the flagellum. The tangent angle of the flagellum can be decomposed by the zeroth and first Fourier coefficients as follows³¹:

$$\varphi(s, t) \approx \phi(s) + \psi(s)e^{i\omega t} + \psi^*(s)e^{-i\omega t}, \quad (2)$$

where $\phi(s)$ is the zeroth mode and characterizes the time-

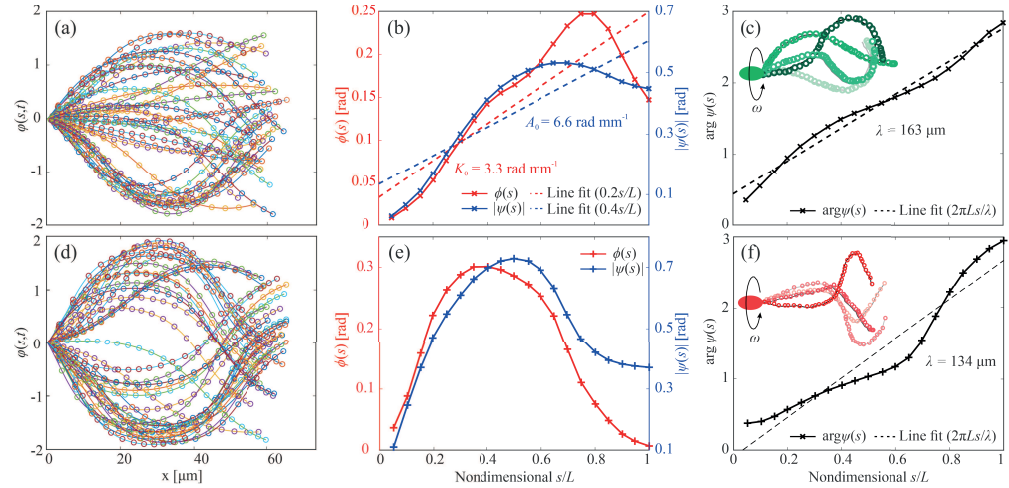


FIG. 2. Flagellar waveforms of motile and magnetically-actuated sperm cells are characterized. (a) The tangent angle ($\varphi(s, t)$) is determined from the flagellar deformation across a complete beat cycle. (b) The mean flagellar curvature is 3.3 rad mm^{-1} , whereas the amplitude rise is 6.6 rad mm^{-1} . (c) $\lambda = 163 \text{ }\mu\text{m}$. (d) The tangent angle of a magnetically-actuated sperm cell. (e) The curvature increases and decreases along the flagellum, while the maximum amplitude occurs at $0.5L$ from the proximal end of the cell. (f) $\lambda = 134 \text{ }\mu\text{m}$. Insets show the measured waveforms over half beat cycle. Darker curves indicate later times.

averaged mean shape of the flagellum. Further, $\psi(s)$ and $\psi^*(s)$ are the first mode and its complex conjugate, and its magnitude characterizes the bending amplitude along the flagellum. Equation (1) gives the following relation between the hydrodynamic and magneto-elastic coupling:

$$-\frac{i}{\ell_\omega^4}(\psi e^{i\omega t} - \psi^* e^{-i\omega t}) = \frac{\partial^4 \phi}{\partial s^4} + \frac{\partial^4 \psi}{\partial s^4} e^{i\omega t} + \frac{\partial^4 \psi^*}{\partial s^4} e^{-i\omega t}, \quad (3)$$

where $\ell_\omega = (\kappa/\omega\xi_\perp)^{1/4}$ is the characteristic penetration length³². The hydrodynamics can be simplified by using ideal flagellar waveform. Riedel-Kruse *et al.* have shown that the ideal flagellar waveform consists of an arc with constant curvature ($\phi(s) = K_0 s$) and a bending amplitude that increases along the flagellum linearly ($\psi(s) = A_0 s$), where K_0 and A_0 are the curvature and the bending amplitude of the flagellum, respectively³¹. Under these conditions, we have $\partial^4 \phi/\partial s^4 = 0$, $\partial^4 \psi/\partial s^4 = 0$, and $\partial^4 \psi^*/\partial s^4 = 0$. In addition, since the characteristic penetration length is nonzero for nonzero actuation frequency $\omega = 2\pi f$, we obtain

$$\text{Re}\{\psi(s)\} \sin \omega t + \text{Im}\{\psi(s)\} \cos \omega t = 0. \quad (4)$$

Equation (4) defines the phase angle, $\Phi = -\arg\psi(s)$ which characterizes the progression of the wave along the flagellum. The tangent angle is determined using the measured flagellum deformation (Fig. 2(a)) and the zeroth and first Fourier modes are calculated using equation (2). The zeroth coefficient $\phi(s)$ for an active flagellum is used to determine K_0 by fitting a line to the

data, as shown in Fig. 2(b). Similarly to the curvature, A_0 is determined by fitting a line to $|\psi(s)|$. Therefore, K_0 and A_0 of the motile cell in this trial are 3.3 rad mm^{-1} and 6.6 rad mm^{-1} , respectively, and the curvature and bending moment are approximately linear with the exception of the proximal and distal ends. Fig. 2(c) shows the measured phase angle. The wavelength (λ) is determined as $163 \text{ }\mu\text{m}$ by fitting a line $2\pi Ls/\lambda$ to the phase angle, where L is the length of the flagellum. This experiment is implemented using 10 different sperm cells for 3 consecutive periods of motion, and average K_0 , A_0 , and λ are provided in Table II. We repeat the same test for magnetically-actuated sperm cells (Fig. 2(d)). Unlike active flagellum, the curvature of the passive flagellum increases and then decreases toward the distal end, while the maximum amplitude of the bending wave occurs at $0.5L$ from the proximal end (Fig. 2(e)). Therefore, the curvature and bending moment are calculated for, $0 < s < 0.5L$, as $37.4 \pm 18.1 \text{ rad mm}^{-1}$ and $15.9 \pm 7.0 \text{ rad mm}^{-1}$, respectively. The rotation of the magnetic head also induces wave propagation with an average wavelength, $\lambda = 150 \pm 13 \text{ }\mu\text{m}$ (Fig. 2(f)).

Fig. 2(b) shows that the curvature increases linearly, except for the proximal and distal ends of the active flagellum, whereas Fig. 2(e) shows that the curvature increases and then decreases toward the distal end of the passive flagellum. We attribute this behaviour to the difference in actuation, as active flagellum has distributed actuation, whereas passive flagellum is actuated by the exerted magnetic moment at the head only. Further, the

TABLE II. Characterized waveform and motion variables.

Sperm cell	Motile cell	Magnetic cell
K_0 [rad mm ⁻¹]	10.4 ± 8.1	37.4 ± 18.1 ($s \in 0 : 0.5L$)
A_0 [rad mm ⁻¹]	6.7 ± 2.2	15.9 ± 7 ($s \in 0 : 0.5L$)
λ [μ m]	198 ± 44	150 ± 13
VSL [μ m s ⁻¹]	101.6 ± 31.6	6.3 ± 1.2
VCL [μ m s ⁻¹]	225.4 ± 77.1	24.9 ± 14.4
LIN (VSL/VCL)	0.48 ± 0.18	0.28 ± 0.1
VAP [μ m s ⁻¹]	113.2 ± 31.7	7.3 ± 1.1

passive bending stiffness of live spermatozoa depends on the amount of ATP present in the medium²⁶. In case of magnetically-actuated sperm cells, the bending stiffness of the flagellum can not be estimated because the cells are not alive anymore and the state of interaction has not yet been quantified for non-metabolizing sperm cells. Therefore, the difference in flagellar waveform can be attributed to differences between internal and external power generation. Similarly to the curvature, the bending moment along the flagellum is mostly linear in the case of the motile cells, while the magnetically-actuated cells show a decreasing amplitude along the flagellum. The curvature and bending moment also reveal that the asymmetry of the flagellar mean shape is more evident in the case of magnetically-actuated cells. In contrast to the curvature and bending amplitude, the rate of propagation of the elastic wave of the motile and magnetic cells are quite similar (Fig. 2(c) and 2(f)). The average slope of phase angle for the motile cells is $2\pi/\lambda = 2\pi/185$, whereas magnetically-actuated cells have an average slope of $2\pi/134$, at actuation frequency of 6 Hz. Therefore, the magnetic field enables non-motile cells to rotate with respect to \mathbf{e}_1 while displaying helical flagellar waves like motile cells.

The wave variables dictate the time-dependent deformation of the flagellum. Therefore, the force exerted by the flagellum is determined using the resistive-force theory (RFT)^{29,33} for a range of wave variables (Table II). Fig. 3 shows the influence of A_0 and λ on the swimming velocity. The green and red shaded regions indicate the minimum and maximum $F/(\eta\omega A_{\max}^2)$ for motile and magnetic cells, respectively. Equation (2) is integrated to determine the deformation of the flagellum ($y(x, t)$) in the material frame of the cell ($\mathbf{e}_1, \mathbf{e}_2$). The deformation is used to determine the following force using RFT for the tangential (ξ_{\perp}) and perpendicular (ξ_{\parallel}) drag coefficients of Gray and Hancock²⁹ and Lighthill³³:

$$F = \int_0^{\lambda} \left(\frac{(\xi_{\perp} - \xi_{\parallel}) \frac{\partial y}{\partial t} \frac{\partial y}{\partial x} - f\lambda(\xi_{\parallel} + \xi_{\perp} \left(\frac{\partial^2 y}{\partial x^2}\right)^2)}{1 + \left(\frac{\partial^2 y}{\partial x^2}\right)^2} \right) dx. \quad (5)$$

We observe that the wave variables of motile cells generate greater force than magnetically-actuated cells. The cells display a flagellar wave accompanied by a rotation of the body with respect to the long axis of the head (\mathbf{e}_1), and swim along a curved path. This motion is charac-

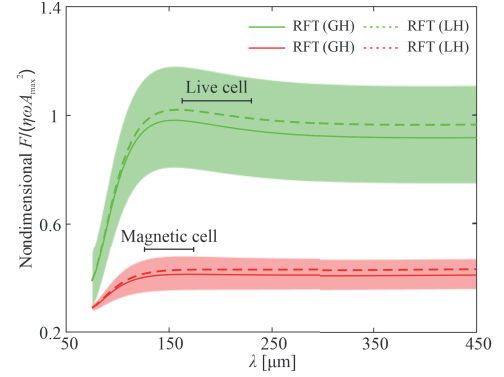


FIG. 3. The thrust force (F) is calculated using (5) based on the average (K_0) and (A_0) for a range of wavelength (λ). The solid and dashed lines indicate average forces calculated by the resistive-force theory (RFT) of Gray and Hancock²⁹ and Lighthill (LH)³³, respectively. η, ω, A_{\max} are the viscosity, frequency, and the maximum amplitude, respectively. Minimum and maximum $F/(\eta\omega A_{\max}^2)$ are calculated using RFT of Gray and Hancock and indicated using the shaded regions.

terized by an average VSL of $101.6 \pm 31.6 \mu\text{m s}^{-1}$ and VCL of $225.4 \pm 77.1 \mu\text{m s}^{-1}$, as shown in Fig. 4 (Multimedia view). A drastic decrease of the swimming speed is observed in the case of magnetically-actuated cells, with average VSL of $6.3 \pm 1.2 \mu\text{m s}^{-1}$ and VCL of $24.9 \pm 14.4 \mu\text{m s}^{-1}$. This decrease is attributed partially to the additional drag exerted on the nanoparticle aggregates that coat the sperm head. The swimming velocity of the cell is dictated by the asymptotic force balance between the thrust force generated by the tail and the drag force on the head. Regardless of the difference in swimming speed which is attributed to the calculated thrust force (Fig. 3), the average LIN indicates another fundamental difference in flagellar propulsion. The average linearity is 0.48 ± 0.18 and 0.28 ± 0.1 for motile and magnetically-actuated sperm cells, respectively. The curvature of the paths taken by magnetically-actuated sperm cells is larger than motile cells. Figs. 2(b) and 2(e) show the asymmetry of the mean shape. This asymmetry is noticeable in the case of magnetically-actuated cells, leading to greater deviation between VSL and VCL. The insets in Fig. 2(c) and 2(f) show the flagellar waveform. These waveforms indicate qualitatively that the asymmetry is more noticeable for magnetically-actuated sperm cells, leading to lower LIN.

In this letter, we show the influence of distributed bending and localized external actuation of motile and non-motile cells, respectively. Waveform analysis reveals that maximum amplitude of the bending wave occurs at $0.75L$ and $0.5L$ from the proximal end of the active and passive flagellum, respectively, leading to greater swimming speed of the motile cells. Therefore, the actuation of the passive flagellum at the proximal end does

This is the author's peer reviewed, accepted manuscript. However, the online version of record will be different from this version once it has been copyedited and typeset.

PLEASE CITE THIS ARTICLE AS DOI: 10.1063/1.5142470

Similarities between Active and Magnetically-Actuated Flagella of Sperm Cells

5

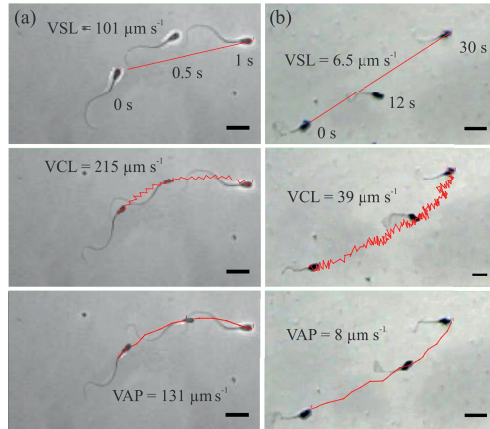


FIG. 4. Trajectories of motile and magnetically-actuated sperm cells. (a) Straight line velocity (VSL), curvilinear velocity (VCL) and average path velocity (VAP) for motile bull sperm. (b) VSL, VCL, and VAP are calculated from magnetically-actuated sperm cells. Scale bars are 20 μm . ([Multimedia view](#))

not resemble the distributed actuation of the flagellum. However, the incorporation of nanoparticles opens up additional possibilities to resemble waveform patterns of motile cells, such as the use of different nanoparticles that will selectively adhere to certain locations along the flagellum, enabling non-uniform distributed actuation. In conclusion, this work contributes to the understanding of how motile sperm cells perform their efficient motion in low- Re . The actuation of a passive flagellum enables us to understand how to design efficient microswimmers. It would be essential to dope the non-motile cells with different magnetic entities on different locations. Further, a combination of attractive and repulsive particles might enlarge the amplitude of flagellar wave toward the distal end and enhance the propulsion. This would also mimic the interactions of molecular motors of sperm cells. This work was supported in part by the European Research Council (ERC) through the European Unions Horizon 2020 Research and Innovation Program under Grant 638428 (Project ROBOTAR). This work was also supported by the Zukunftskonzept of the TU Dresden, funded by the excellence initiative of the German Research Foundation (DFG) and the Volkswagen foundation, grant nr91619.

¹L. Zhang, J. J. Abbott, L. Dong, B. E. Kratochvil, D. Bell, and B. J. Nelson, *Applied Physics Letters* **94**, 064107 (2009).

²K. E. Peyer, L. Zhang, and B. J. Nelson, *Nanoscale* **5**, 1259–1272 (2012).

³A. Ghosh and P. Fischer, *Nano Letters* **9**, 2243–2245 (2009).

⁴B. Behkam and M. Sitti, *Applied Physics Letters* **90**, 023902 (2007).

⁵V. Magdanz, S. Sanchez, and O. G. Schmidt, *Advanced Materials* **25**, 6581–6588 (2013).

⁶B. J. Williams, S. V. Anand, J. Rajagopalan, and M. T. A. Saif, *Nature* **5**, 3081 (2014).

⁷R. Dreyfus, J. Baudry, M. L. Roper, M. Fermigier, H. A. Stone, and J. Bibette, *Nature* **437**, 862–865 (2006).

⁸M. P. Kummer, J. J. Abbott, B. E. Kartochvil, R. Borer, A. Sengul, and B. J. Nelson, *IEEE Transactions on Robotics* **26**, 1006–1017 (2010).

⁹O. S. Pak, W. Gao, J. Wang, and E. Lauga, *Soft Matter* **7**, 8169–8181 (2011).

¹⁰G. Adam, S. Chowdhury, M. Guix, B. Johnson, C. Bi, and D. Cappelleri, *Robotics* **8**, 69 (2019).

¹¹J. Li, T. Li, T. Xu, M. Kiristi, W. Liu, Z. Wu, and J. Wang, *Nano Letters* **15**, 4814–4821 (2015).

¹²S. Palagi, A. G. Mark, S. Y. Reigh, K. Melde, T. Qiu, H. Zeng, C. Parmeggiani, D. Martella, A. Sanchez-Castillo, N. Kapernaum, F. Giesselmann, D. S. Wiersma, E. Lauga, and P. Fischer, *Nature Materials* **15**, 647–653 (2016).

¹³W. F. Paxton, K. C. Kistler, C. C. Olmeda, A. Sen, S. K. S. Angelo, Y. Cao, T. E. Mallouk, P. E. Lammert, and V. H. Crespi, *Journal of the American Chemical Society* **12**, 13424–13431 (2004).

¹⁴S. Fournier-Bidoz, A. C. Arsenault, I. Manners, and G. A. Ozin, *Chemical Communication* **441**, 441–443 (2004).

¹⁵J. J. Abbott, K. E. Peyer, L. Dong, and B. Nelson, *The International Journal of Robotics Research* **28**, 1434–1447 (2009).

¹⁶I. S. M. Khalil, H. C. Dijkslag, L. Abelmann, and S. Misra, *Applied Physics Letters* **104**, 174101 (2014).

¹⁷E. M. Purcell, *American J. Physics* **45**, 3–11 (1977).

¹⁸R. W. Carlsen, M. R. Edwards, J. Zhuang, C. Pacoret, and M. Sitti, *Lab on a Chip* **14**, 3850–3859 (2014).

¹⁹X. Yan, Q. Zhou, M. Vincent, Y. Deng, J. Yu, J. Xu, T. Xu, T. Tang, L. Bian, Y.-X. J. Wang, K. Kostarelos, and L. Zhang, *Science Robotics* **2**, eaaq1155 (2017).

²⁰V. Magdanz, M. Medina-Sánchez, L. Schwarz, H. Xu, J. Elgeti, and O. G. Schmidt, *Advanced Materials* **29**, 1606301 (2017).

²¹H. Xu, M. Medina-Sánchez, V. Magdanz, L. Schwarz, F. Hebenstreit, and O. G. Schmidt, *ACS Nano* **12**, 327–337 (2018).

²²J.-J. Chung, S.-H. Shim, R. A. Everley, S. P. Gygi, X. Zhuang, and D. E. Clapham, *Cell* **157**, 808–822 (2014).

²³B. M. Friedrich and F. Jülicher, *PNAS* **104**, 13256–13261 (2007).

²⁴A. G. A. Bahat, I. Tur-Kaspa, L. C. Giojalas, H. Breitbart, and M. Eisenbach, *Nature Medicine* **9**, 149–150 (2003).

²⁵C. Chen, X. Chang, P. Angsantikul, J. Li, B. E.-F. de Ávila, E. Karshalev, W. Liu, F. Mou, S. He, R. Castillo, J. G. Y. Liang, L. Zhang, and J. Wang, *Advanced Biosystems* **2**, 1700160 (2018).

²⁶C. B. Lindemann and K. A. Lesich, *Journal of Cell Science* **123**, 519–528 (2010).

²⁷W. H. Organization, *WHO laboratory manual for the Examination and processing of human semen*, 5th ed. (World Health Organization, 20 Avenue Appia, 1211 Geneva 27, Switzerland, 2010).

²⁸V. Magdanz, J. Gebauer, P. S. Abd S. Eltoukhy, D. Voigt, and J. Simmchen, *Advanced Biosystems* **3**, 1900061 (2019).

²⁹J. Gray and G. J. Hancock, *Journal of Experimental Biology* **32**, 802–814 (1955).

³⁰K. E. Machin, *Journal of Experimental Biology* **35**, 796–806 (1958).

³¹B. M. Friedrich, I. H. Riedel-Kruse, J. Howard, and F. Jülicher, *The Journal of Experimental Biology* **213**, 1226–1234 (2010).

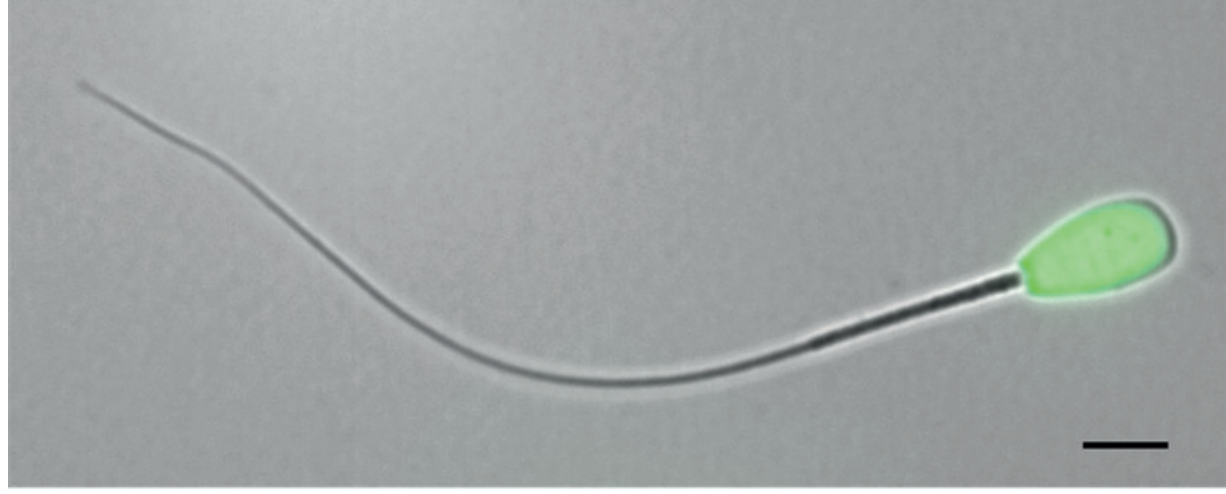
³²E. L. Tony S. Yu and A. E. Hosoi, *Physics of Fluids* **18**, 091701 (2006).

³³J. Lighthill, *SIAM Review* **18**, 161–230 (1976).

³⁴K. A. Lesich, D. W. Pelle, and C. B. Lindemann, *Biophysical Journal* **95**, 472–482 (2008).

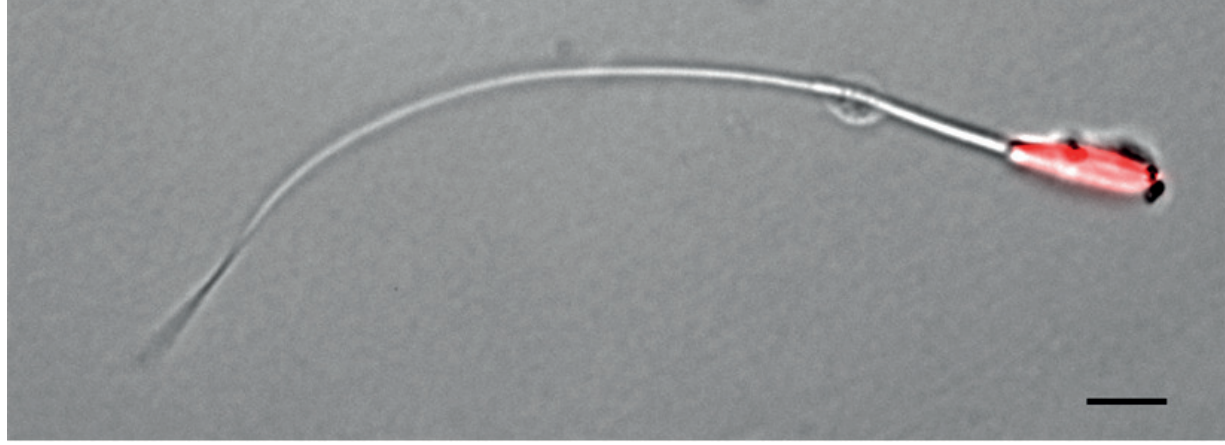
This is the author's peer reviewed, accepted manuscript. However, the online version of record will be different from this version once it has been copyedited and typeset.

PLEASE CITE THIS ARTICLE AS DOI: 10.1063/1.5142470



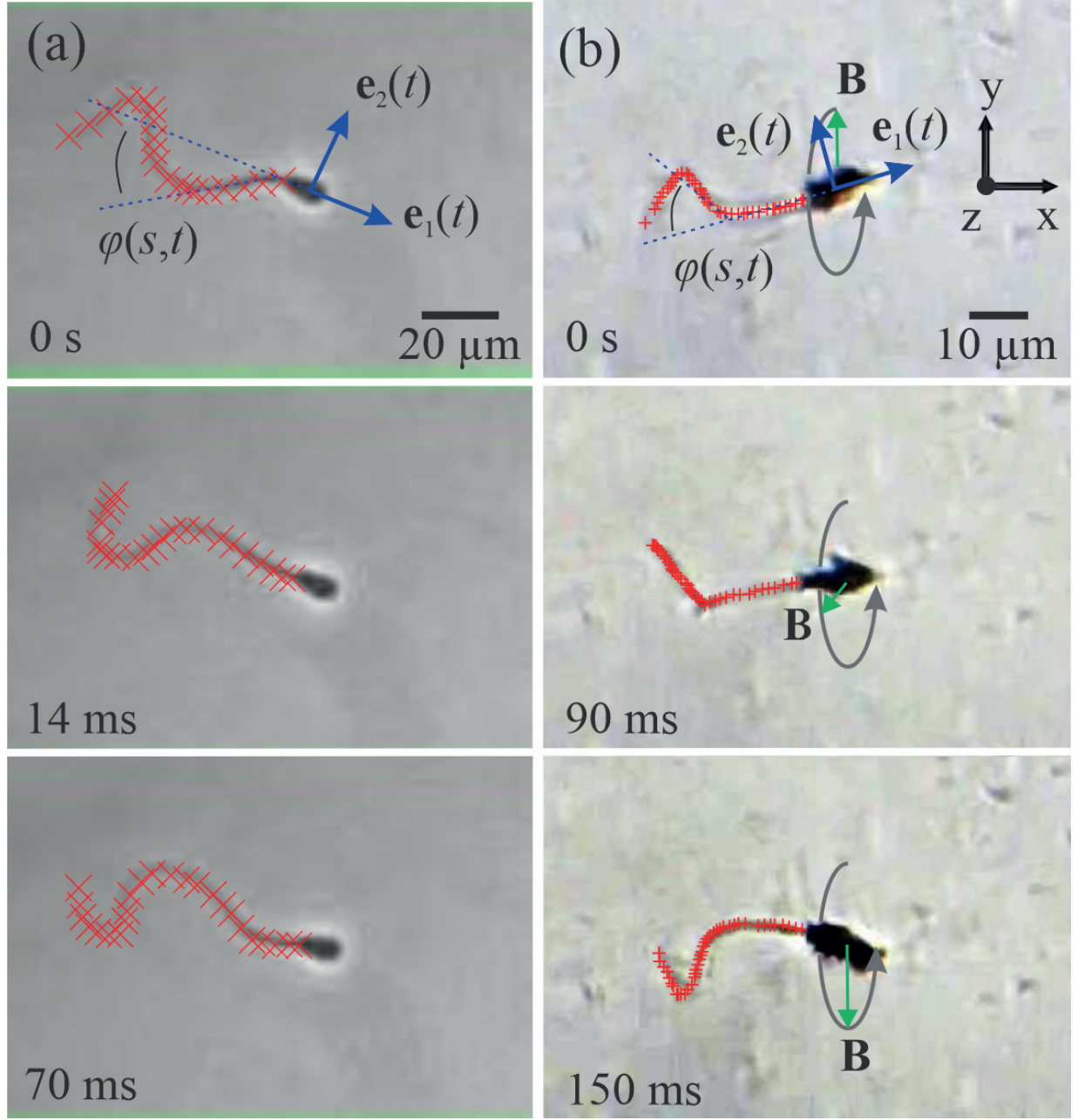
This is the author's peer reviewed, accepted manuscript. However, the online version of record will be different from this version once it has been copyedited and typeset.

PLEASE CITE THIS ARTICLE AS DOI: 10.1063/1.5142470



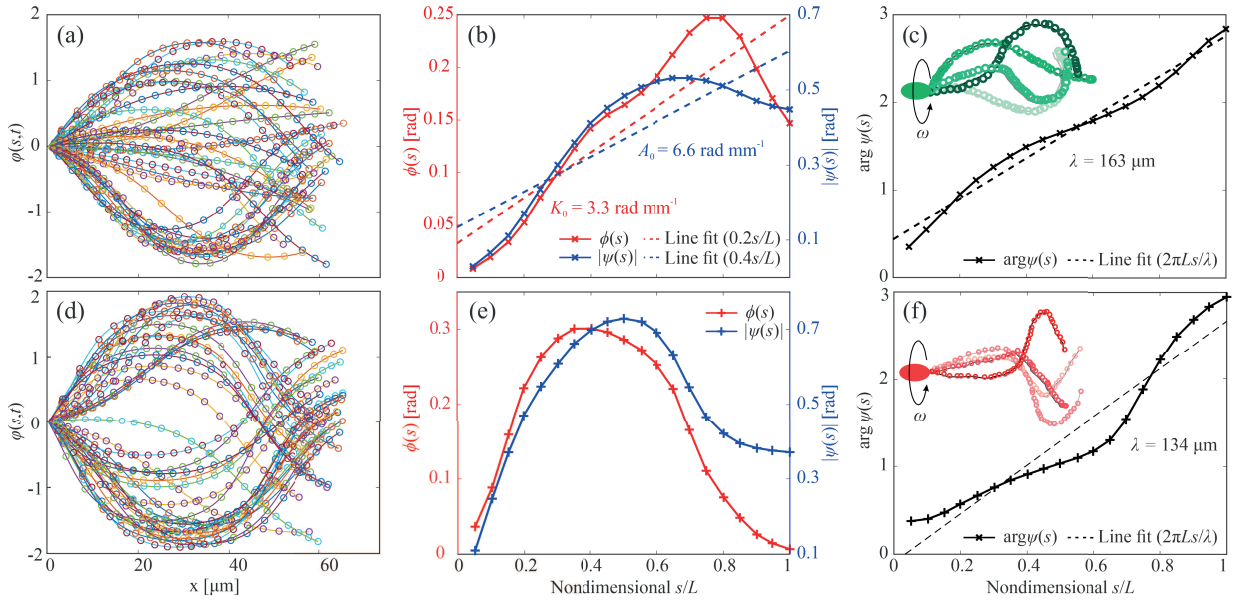
This is the author's peer reviewed, accepted manuscript. However, the online version of record will be different from this version once it has been copyedited and typeset.

PLEASE CITE THIS ARTICLE AS DOI: 10.1063/1.5142470



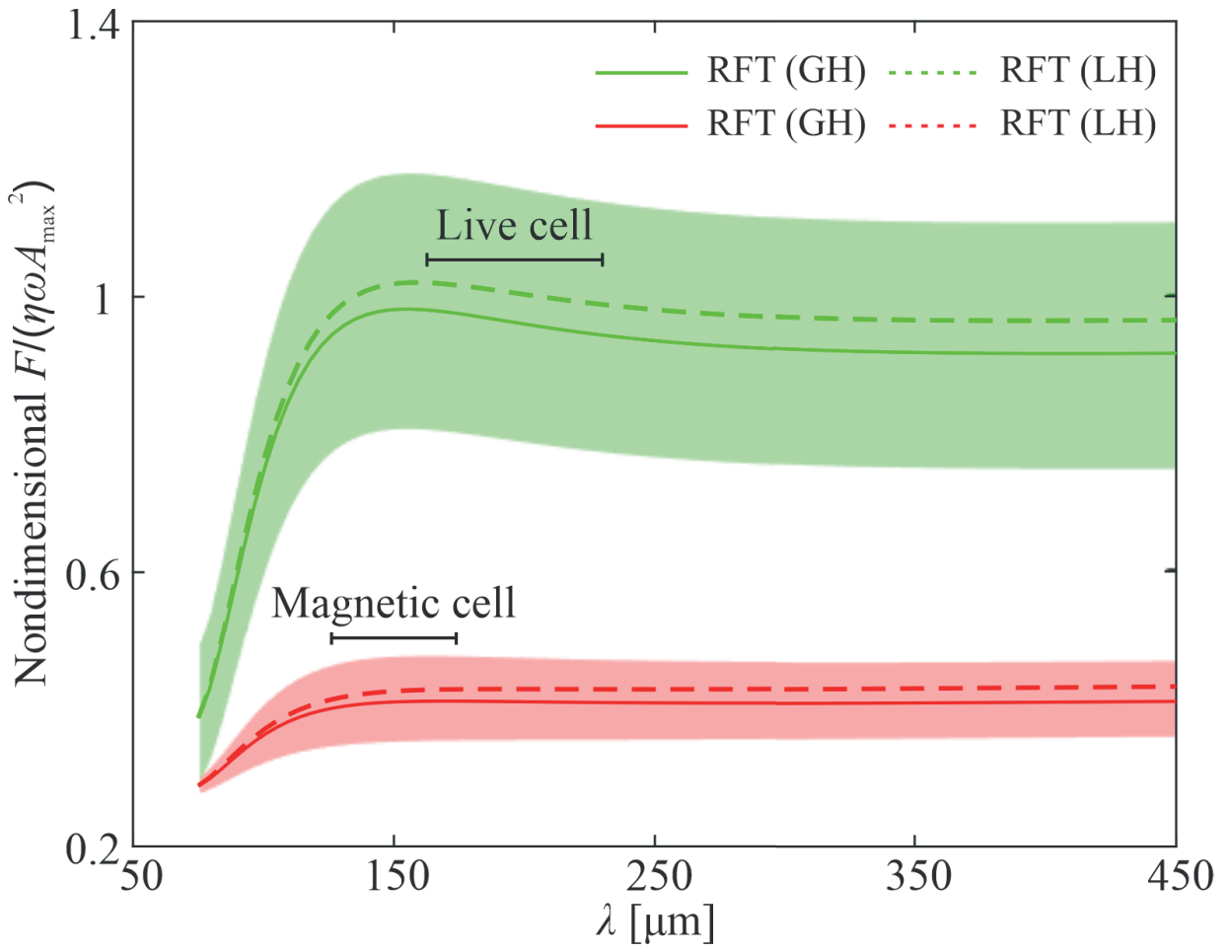
This is the author's peer reviewed, accepted manuscript. However, the online version of record will be different from this version once it has been copyedited and typeset.

PLEASE CITE THIS ARTICLE AS DOI: 10.1063/1.5142470



This is the author's peer reviewed, accepted manuscript. However, the online version of record will be different from this version once it has been copyedited and typeset.

PLEASE CITE THIS ARTICLE AS DOI: 10.1063/1.5142470



This is the author's peer reviewed, accepted manuscript. However, the online version of record will be different from this version once it has been copyedited and typeset.

PLEASE CITE THIS ARTICLE AS DOI: 10.1063/1.5142470

